# Apertureless near-field terahertz imaging using the self-mixing effect in a quantum cascade laser

Paul Dean,[1,a)] Oleg Mitrofanov,[2] James Keeley,[1] Iman Kundu,[1] Lianhe Li,[1] Edmund H. Linfield,[1] and A. Giles Davies[1]
[1]School of Electronic and Electrical Engineering, University of Leeds, Leeds LS2 9JT, United Kingdom
[2]Department of Electronic and Electrical Engineering, University College London, Torrington Place, London WC1E 7JE, United Kingdom

(Received 5 November 2015; accepted 19 February 2016; published online 4 March 2016)

We report two-dimensional apertureless near-field terahertz (THz) imaging using a quantum cascade laser (QCL) source and a scattering probe. A near-field enhancement of the scattered field amplitude is observed for small tip-sample separations, allowing image resolutions of $\sim 1\,\mu$m ($\sim\lambda/100$) and $\sim 7\,\mu$m to be achieved along orthogonal directions on the sample surface. This represents the highest resolution demonstrated to date with a THz QCL. By employing a detection scheme based on self-mixing interferometry, our approach offers experimental simplicity by removing the need for an external detector and also provides sensitivity to the phase of the reinjected field. © *2016 Author(s). All article content, except where otherwise noted, is licensed under a Creative Commons Attribution 3.0 Unported License*. [http://dx.doi.org/10.1063/1.4943088]

Near-field terahertz (THz) imaging[1] techniques have shown great potential for the investigation of solid-state and organic systems exhibiting features on sub-wavelength scales. Applications of near-field THz imaging reported to date include the mapping of charge carriers in semiconductors and nanostructures,[2,3] investigation of metamaterials,[4,5] characterisation of THz waveguides,[6,7] and THz microscopy of biomedical samples.[8] Within this field, a number of approaches have been employed to overcome the diffraction limit imposed by traditional far-field imaging techniques. A sub-wavelength aperture, or aperture-like probe, can be used to restrict the illuminating beam spatially or limit the detection area in the near-field.[9–12] However, the achievable resolution and dynamic range of this approach are often limited by the strong beam attenuation arising from the aperture. Similarly, enhanced near-field sensitivity can be accomplished by placing the source or detector in close proximity to the sample under investigation,[13–15] although implementation can be experimentally challenging. An alternative technique for the THz range has been adapted from apertureless (scattering-type) near-field scanning optical microscopy (ANSOM).[2,3,16–18] In this implementation, a scattering probe, positioned close to the sample, is illuminated and the scattered field collected in the far-field. The near-field interaction between the probe tip and sample surface causes a modification to the phase and amplitude of the scattered field, enabling the local optical properties of the sample to be probed with a spatial resolution determined by the tip radius, independent of the radiation wavelength.

Whilst the majority of THz near-field imaging systems have employed a broadband source, the THz-frequency quantum cascade laser (QCL)[19] represents an attractive alternative owing to its compact size, broad spectral coverage,[20,21] and high output power.[22] Nevertheless, to date, near-field imaging has been demonstrated only using aperture-based approaches,[23,24] with the highest resolution reaching only $\sim 10\,\mu$m ($\sim\lambda/10$). In this letter, we report apertureless near-field imaging using a scattering probe and a QCL source emitting at 2.53 THz. We observe a near-field enhancement of the scattered field amplitude for small tip-sample separations, and achieve image resolutions of $\sim 1\,\mu$m ($\sim\lambda/100$) and $\sim 7\,\mu$m along orthogonal directions on the sample surface. By employing a detection scheme based on self-mixing (SM) interferometry,[25] thereby removing the need for an external THz detector, our approach offers a compact and simple semiconductor-based platform for near-field THz imaging. The coherent nature of this scheme also allows both the phase and amplitude of the scattered field to be resolved without the need for an external interferometer[2] or synchronisation of the source to an ultrafast laser.[3,4] Furthermore, this detection approach is intrinsically fast, since it is fundamentally limited by electron transport in the QCL, and is therefore suited to fast image acquisition.[26]

The imaging system used in this work was adapted from that described in Ref. 25. The THz QCL consisted of a 10–$\mu$m-thick bound-to-continuum active region[27] emitting at 2.53 THz ($\lambda \approx 119\,\mu$m), and was processed into a surface-plasmon ridge waveguide with dimensions 2.4 mm × 150 $\mu$m. The device was cooled using a continuous flow helium cryostat and maintained at a constant heat-sink temperature of 25 K. A current source was used to drive the laser at a constant current of 945 mA. Radiation from the laser was focused onto the tip of a horizontally oriented (parallel to the $z$-axis) platinum-iridium needle using a pair of 2-in.-diameter $f/2$ off-axis parabolic reflectors, with the beam axis forming an elevation angle $\theta \sim 50°$ relative to the needle shaft (see Fig. 1). The needle diameter was 0.5 mm, and the tip was mechanically polished to form a tip radius smaller than 1 $\mu$m. The length of the external cavity formed between the tip and the QCL facet was $L_0 = 40$ cm. A vertically oriented (in the $x-y$ plane) sample, mounted on a three-axis computer-controlled translation stage, was positioned in proximity to the needle tip at a separation $d$. In this configuration, the incident THz field contains

a)Electronic mail: p.dean@leeds.ac.uk

 

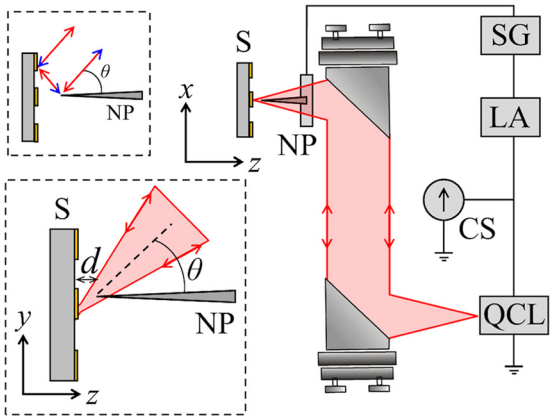


FIG. 1. Schematic diagram of the experimental system. S: Sample; NP: needle probe mounted on piezoelectric transducer; CS: current source; LA: lock-in amplifier; SG: signal generator. Radiation from the QCL is focused onto the tip of the scattering needle probe using a parabolic reflector, with the beam axis forming an elevation angle $\theta \sim 50°$ relative to the shaft of the needle (see bottom-left inset). The needle tip is dithered sinusoidally in the $z$-direction. Top-left inset: Geometry in which illumination of the tip (blue arrow heads) and/or collection of the scattered field (red arrows) occurs via a surface reflection from the sample.

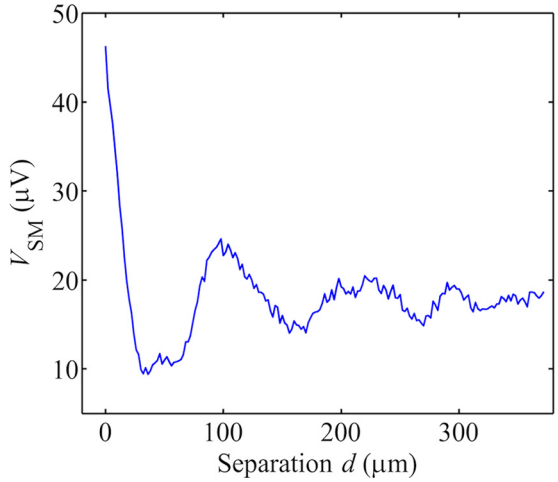


FIG. 2. Self-mixing voltage $V_{SM}$ recorded as a function of tip-sample separation $d$, with the needle tip modulated at 90 Hz with amplitude $\sim 1\,\mu$m. A near-field enhancement of the signal is observed for small separations. A background signal is observed with oscillations on a length-scale dependent on the system geometry. The $d = 0\,\mu$m position represents a nominal zero tip-sample separation (and was identified by visual inspection with a $\times 25$ objective lens).

both s- and p-polarisation components with respect to the sample, and the focused beam spot size is estimated to be $\sim 250\,\mu$m. The laser radiation scattered from the tip-sample system was coupled back into the QCL facet along the same optical path as the incident beam, and the resulting SM signal was monitored through the QCL terminal voltage $V_{SM}$.

The reinjected THz field $E_{tot}$ mixes with the QCL intracavity field, producing a perturbation to the laser voltage that depends on both the amplitude and phase of the THz field.[25,28] We can express $E_{tot}$ as a superposition of field components scattered from the needle-sample system according to the equation

$$E_{tot} = E_s + E_b + E_{NF}. \tag{1}$$

In this expression $E_s$ represents the background field arising from radiation scattered directly from the sample surface and reinjected to the laser cavity. To discriminate against this unwanted component, a modulation scheme was employed in which the needle tip was dithered sinusoidally in the $z$-direction at 90 Hz with amplitude $\sim 1\,\mu$m, using a piezoelectric transducer. The synchronised in-phase component of the SM signal was then recovered using a lock-in amplifier referenced to the needle modulation. The second term, $E_b$, relates to background scattering from the needle shaft and tip, including via reflection from the sample surface.[29–31] For a phase-sensitive detection schemes such as that employed here, these background scattered fields will experience phase modulation and will not be suppressed fully by lock-in detection at the fundamental modulation frequency,[29–32] as demonstrated below. The final term $E_{NF}$ accounts for the near-field enhancement of the field scattered by the tip in the presence of a dielectric sample, as discussed below.

In order to clarify these contributions to the reinjected field, the SM signal was monitored as the sample was translated in the $z$-direction (towards the needle tip). Figure 2 shows an exemplar approach curve recorded with a silver mirror as the sample. The $d = 0\,\mu$m position has been defined to represent the nominal zero tip-sample separation, as determined by visual inspection using a remote camera fitted with a $\times 25$ objective lens. At large tip-sample separations a non-zero signal is observed, which can be attributed to contributions to $E_b$ arising from direct scattering from the isolated needle. As the separation $d$ decreases, a series of oscillations are observed in the measured signal. Such effects have been observed in previous ANSOM implementations[29,30] and arise from interference fringes parallel to the sample surface caused by illumination of the tip and/or collection of the scattered field via a surface reflection, as depicted in the inset to Fig. 1. This phenomenon produces variations in $E_b$ on a length-scale dependent on the system geometry and alignment, but of the order $\lambda/2\cos\theta \approx 95\,\mu$m.

As the sample approaches the probe, a sharp increase in the signal is observed in Fig. 2, which can be attributed to a near-field enhancement of the scattering cross-section of the tip-sample system. This effect has been described previously using a coupled dipole model[16,32] that treats the needle tip as a sphere with radius $R$ and polarizability $\alpha$ that is polarised by the incident field $E_0$. This dipole induces an image dipole in the dielectric sample, with permittivity $\varepsilon_s$, which couples with the dipole of the tip yielding an effective polarizability of the tip-sample system given (for p-polarised light) by

$$\alpha_{eff} = \frac{\alpha[1 + (\varepsilon_s - 1)/(\varepsilon_s + 1)]}{1 - \dfrac{\alpha(\varepsilon_s - 1)/(\varepsilon_s + 1)}{16\pi(R + d)^3}}. \tag{2}$$

The total field scattered at the tip varies $\propto \alpha_{eff} E_0$, leading to a significant enhancement of the near-field term, $E_{NF}$, in Eq. (1) as $d$ approaches zero. It should also be noted that, due to the strong nonlinear dependence of the near-field interaction with tip-sample separation, the near-field term $E_{NF}$ can, in principle, be further discriminated against the

unwanted background signal $E_b$ through demodulation at second and higher harmonics of the tip modulation frequency.[29,30,33]

An important consideration in our coherent ANSOM implementation is the effect of the external cavity round-trip phase on the field components appearing in Eq. (1). To investigate this, a series of successive approach curves were recorded for different external cavity lengths. The cavity length was controlled by adjusting the position of the needle tip along the $z$-axis; for an increment of the tip position $\Delta z$ relative to that used in Fig. 2, the path length in the external cavity formed between the tip and the QCL facet decreases from the nominal value $L_0$ by an amount $\Delta L = -\Delta z \cos\theta$. Figure 3 shows approach curves recorded with $\Delta L$ varied from $\Delta L = -10.9\,\mu$m ($\Delta z = 17\,\mu$m) to $\Delta L = -22.5\,\mu$m ($\Delta z = 35\,\mu$m), in steps $\Delta L = -1.9\,\mu$m ($\Delta z = 3\,\mu$m). The signal recorded at large tip-sample separations $d > \lambda$, representing the scattering contribution from the isolated needle, can be seen to vanish with increasing $\Delta L$ within this range. This null in the background signal $E_b$ would occur when the external cavity length satisfies the condition $L_0 = (m \pm 1/4)\lambda/2$, where $m$ is an integer value. Experimentally, the background signal was observed to oscillate between positive and negative peak values, corresponding to cavity lengths $m\lambda/2$ and $(m+1/2)\lambda/2$, respectively, as the tip was translated through the beam. Also evident from Fig. 3 is that the sign of the enhanced near-field signal recorded at $d = 0$ varies similarly with the cavity round-trip phase, with both positive and negative signals being observed depending on the needle position within the beam focus. The largest magnitude of the near-field signal recorded here is $14\,\mu$V (at $\Delta L = -22.5\,\mu$m), although larger values similar to that obtained in Fig. 2 (for which $\Delta L = 0\,\mu$m) were obtained for cavity lengths outside of this range. A null in the near-field signal occurs for $\Delta L \approx -14.8\,\mu$m, which is equivalent to a change in cavity length $\Delta L \approx -\lambda/8$ relative to the cavity length corresponding to a maximum near-field signal, as used in Fig. 2. This is consistent with the expected $\lambda/2$ spacing of the signal maxima, but occurs for a different cavity length than the null in the background signal at $d > \lambda$. This can be explained due to the fact that, for any value of $\Delta L$, there exists a phase mismatch between the field components $E_{NF}$ and $E_b$ in Eq. (1), due to the complex nature of the sample permittivity. Such phase differences have been observed in previously reported ANSOM implementations, in which the near-field phase was also shown to vary with sample composition.[29]

Two-dimensional imaging was demonstrated using a quartz target patterned with a 2 mm × 5 mm rectangular region of 115-nm-thick gold, defined by photolithography. The target was positioned close to the needle tip ($d \approx 0\,\mu$m), and the external cavity length finely adjusted to provide the maximum signal on the lock-in amplifier (i.e., $\Delta L = 0\,\mu$m). A corner of the gold-coated region was then raster-scanned in the $x$–$y$ plane underneath the tip, and $V_{SM}$ recorded at each pixel. A step size of 1 $\mu$m was used, limited by the resolution of the motion control hardware. Figure 4(a) shows an exemplar image, revealing clear contrast between quartz and gold regions of the target. An AFM image of the same region of the sample is shown for comparison in Fig. 4(b). This image reveals roughness of the edges due to delamination of the metal over length scales up to ~2 $\mu$m and ~5 $\mu$m in the $x$ and $y$ directions, respectively. To determine the image

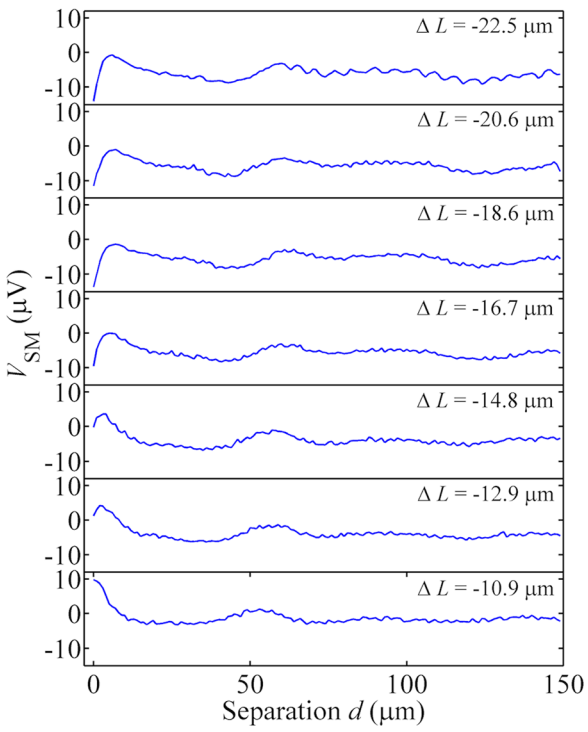


FIG. 3. Self-mixing voltage $V_{SM}$ recorded as a function of tip-sample separation $d$, for different external cavity lengths, varying (bottom to top) from $\Delta L = -10.9\,\mu$m ($\Delta z = 17\,\mu$m) to $\Delta L = -22.5\,\mu$m ($\Delta z = 35\,\mu$m) in steps $\Delta L = -1.9\,\mu$m ($\Delta z = 3\,\mu$m).

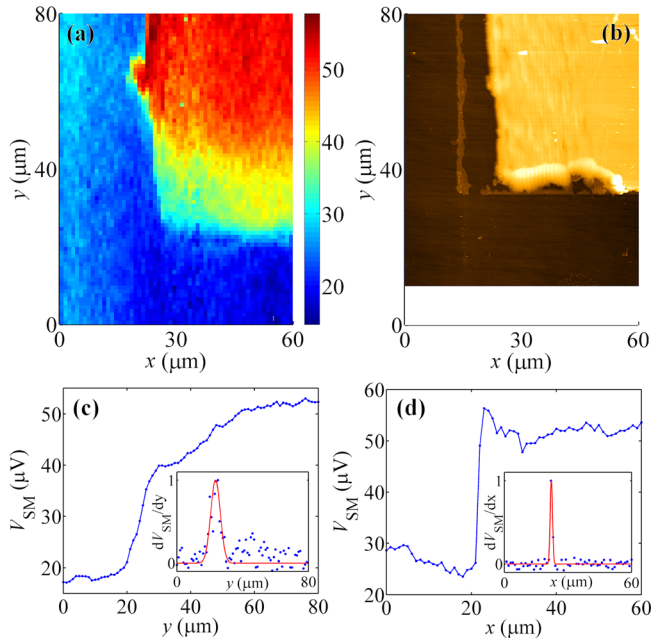


FIG. 4. (a) Two-dimensional near-field image of the corner of a rectangular region of 115-nm-thick gold deposited on a quartz substrate. The colour scale corresponds to the magnitude of $V_{SM}$. (b) AFM image of the same region of the sample. (c) and (d) The ERFs extracted from (a) by averaging seven adjacent rows of pixels ($y = 74$–$80$ $\mu$m and $x = 54$–$60$ $\mu$m, respectively) traversing the edge of the gold-coated region along the $x$ and $y$ directions. The insets show the corresponding spatial derivatives of the ERFs, which have been fitted to a Gaussian function.

resolution, the edge response functions (ERFs) along orthogonal directions were extracted by averaging seven adjacent rows of pixels traversing the edge of the gold-coated region along the $x$ and $y$ directions. The sampled regions were selected to correspond to the minimum edge roughness ($\sim 1\ \mu$m), as determined from Fig. 4(b). Figures 4(c) and 4(d) show these ERFs, respectively, along with their first-order spatial derivatives. From the full-width-at-half-maximum of these derivative functions, the spatial resolutions obtained for the $x$ and $y$ directions are $\sigma_x \approx 1\ \mu$m and $\sigma_y \approx 7\ \mu$m, respectively. This value of $\sigma_x$ is consistent with the nominal tip diameter, which typically determines the achievable image resolution in apertureless near-field imaging systems,[2] and represents a resolution $\sim\lambda/100$ in our case. The inferior resolution obtained in the $y$-direction could be explained by radiation illuminating the tip via a surface reflection, or by radiation launching a THz surface wave at the metallic edge oriented perpendicular to the incident field.[34] Due to the illumination geometry in our system, the presence of such reflections and surface waves would result in a contribution to the scattered field that is sensitive to the optical properties of the sample outside the near-field of the tip and would cause a smearing of the ERF obtained along that direction. Such effects would be present in any ANSOM system employing such an illumination geometry, and do not relate specifically to the SM detection scheme employed here. Alternatively, this inferior resolution could indicate a non-perfect alignment of the sample surface in the $x$–$y$ plane.

In summary, we have reported THz apertureless near-field imaging using a QCL source and a coherent detection scheme based on self-mixing interferometry. We have exploited the near-field enhancement of the scattered field amplitude to demonstrate two-dimensional imaging of exemplar targets, achieving image resolutions of $\sim 1\ \mu$m ($\sim\lambda/100$) and $\sim 7\ \mu$m along orthogonal directions of the sample. This represents the highest image resolution achieved with a THz frequency QCL to date. Our scheme offers an experimentally simple and compact approach to coherent, high-resolution imaging of structures at THz frequencies.

This work was supported by Engineering and Physical Sciences Research Council (EPSRC) Grant COTS (EP/J017671/1). We also acknowledge support from the Royal Society (UF130493) and the Royal Society Wolfson Research Merit Award scheme (AGD, EHL). P.D. acknowledges support from the EPSRC Fellowship scheme (EP/J002356/1). Data associated with this paper are openly available from the University of Leeds data repository: http://doi.org/10.5518/20.

[1]A. Adam, J. Infrared, Millimeter, Terahertz Waves **32**, 976 (2011).
[2]A. J. Huber, F. Keilmann, J. Wittborn, J. Aizpurua, and R. Hillenbrand, Nano Lett. **8**, 3766 (2008).
[3]F. Buersgens, R. Kersting, and H.-T. Chen, Appl. Phys. Lett. **88**, 112115 (2006).
[4]G. Acuna, S. F. Heucke, F. Kuchler, H. T. Chen, A. J. Taylor, and R. Kersting, Opt. Express **16**, 18745 (2008).
[5]A. Bitzer, H. Merbold, A. Thoman, T. Feurer, H. Helm, and M. Walther, Opt. Express **17**, 3826 (2009).
[6]O. Mitrofanov, T. Tan, P. R. Mark, B. Bowden, and J. A. Harrington, Appl. Phys. Lett. **94**, 171104 (2009).
[7]K. Nielsen, H. K. Rasmussen, A. J. Adam, P. C. Planken, O. Bang, and P. U. Jepsen, Opt. Express **17**, 8592 (2009).
[8]C.-M. Chiu, H.-W. Chen, Y.-R. Huang, Y.-J. Hwang, W.-J. Lee, H.-Y. Huang, and C.-K. Sun, Opt. Lett. **34**, 1084 (2009).
[9]S. Hunsche, M. Koch, I. Brener, and M. C. Nuss, Opt. Commun. **150**, 22 (1998).
[10]O. Mitrofanov, I. Brener, M. C. Wanke, R. R. Ruel, J. D. Wynn, A. J. Bruce, and J. Federici, Appl. Phys. Lett. **77**, 591 (2000).
[11]O. Mitrofanov, I. Brener, R. Harel, J. D. Wynn, L. N. Pfeiffer, K. W. West, and J. Federici, Appl. Phys. Lett. **77**, 3496 (2000).
[12]Y. Kawano and K. Ishibashi, Nat. Photonics **2**, 618 (2008).
[13]R. Lecaque, S. Grésillon, and C. Boccara, Opt. Express **16**, 4731 (2008).
[14]M. A. Seo, A. J. L. Adam, J. H. Kang, J. W. Lee, S. C. Jeoung, Q. H. Park, P. C. M. Planken, and D. S. Kim, Opt. Express **15**, 11781 (2007).
[15]A. Bitzer and M. Walther, Appl. Phys. Lett. **92**, 231101 (2008).
[16]B. Knoll and F. Keilmann, Nature **399**, 134 (1999).
[17]H.-T. Chen, R. Kersting, and G. C. Cho, Appl. Phys. Lett. **83**, 3009 (2003).
[18]H. G. von Ribbeck, M. Brehm, D. W. van der Weide, S. Winnerl, O. Drachenko, M. Helm, and F. Keilmann, Opt. Express **16**, 3430 (2008).
[19]M. S. Vitiello, G. Scalari, B. Williams, and P. De Natale, Opt. Express **23**, 5167 (2015).
[20]G. Scalari, C. Walther, M. Fischer, R. Terazzi, H. E. Beere, D. A. Ritchie, and J. Faist, Laser Photonics Rev. **3**, 45 (2008).
[21]C. W. I. Chan, Q. Hu, and J. L. Reno, Appl. Phys. Lett. **101**, 151108 (2012).
[22]L. Li, L. Chen, J. Zhu, J. Freeman, P. Dean, A. Valavanis, A. G. Davies, and E. H. Linfield, Electron. Lett. **50**, 309 (2014).
[23]R. Degl'Innocenti, M. Montinaro, J. Xu, V. Piazza, P. Pingue, A. Tredicucci, F. Beltram, H. E. Beere, and D. A. Ritchie, Opt. Express **17**, 23785 (2009).
[24]A. J. Baragwanath, J. R. Freeman, A. J. Gallant, J. A. Zeitler, H. E. Beere, D. A. Ritchie, and J. M. Chamberlain, Opt. Lett. **36**, 2393 (2011).
[25]P. Dean, Y. L. Lim, A. Valavanis, R. Kliese, M. Nikolić, S. P. Khanna, M. Lachab, D. Indjin, Z. Ikonić, P. Harrison, A. D. Rakić, E. H. Linfield, and A. G. Davies, Opt. Lett. **36**, 2587 (2011).
[26]Y. Ren, R. Wallis, D. S. Jessop, R. Degl'Innocenti, A. Klimont, H. E. Beere, and D. A. Ritchie, Appl. Phys. Lett. **107**, 011107 (2015).
[27]S. Barbieri, J. Alton, H. E. Beere, J. Fowler, E. H. Linfield, and D. A. Ritchie, Appl. Phys. Lett. **85**, 1674 (2004).
[28]P. Dean, A. Valavanis, J. Keeley, K. Bertling, Y. Leng Lim, R. Alhathlool, S. Chowdhury, T. Taimre, L. H. Li, D. Indjin, S. J. Wilson, A. D. Rakić, E. H. Linfield, and A. Giles Davies, Appl. Phys. Lett. **103**, 181112 (2013).
[29]R. Hillenbrand and F. Keilmann, Phys. Rev. Lett. **85**, 3029 (2000).
[30]M. B. Raschke and C. Lienau, Appl. Phys. Lett. **83**, 5089 (2003).
[31]V. Astley, H. Zhan, R. Mendis, and D. M. Mittleman, J. Appl. Phys. **105**, 113117 (2009).
[32]B. Knoll and F. Keilmann, Opt. Commun. **182**, 321 (2000).
[33]K. Moon, H. Park, J. Kim, Y. Do, S. Lee, G. Lee, H. Kang, and H. Han, Nano Lett. **15**, 549 (2015).
[34]R. Mueckstein, C. Graham, C. Renaud, A. Seeds, J. Harrington, and O. Mitrofanov, J. Infrared, Millimeter, Terahertz Waves **32**, 1031 (2011).